Chiral surface and hinge states in higher-order Weyl semimetallic circuits

S. M. Rafi-Ul-Islam,[1,*] Zhuo Bin Siu,[1,†] Haydar Sahin,[1,2,‡] and Mansoor B. A. Jalil[1,§]
[1]*Department of Electrical and Computer Engineering, National University of Singapore, Singapore, Republic of Singapore 117583*
[2]*Institute of High Performance Computing, A*STAR, Singapore, Republic of Singapore 138632*

(Received 19 June 2022; accepted 2 February 2024; published 23 February 2024)

We propose a 3D topolectrical network that can be tuned to realize various higher-order topological gapless and chiral phases. We first study a higher-order Dirac semimetal phase that exhibits a hinge-like Fermi arc linking the Dirac points. This circuit can be extended to host highly tunable first- and second-order Weyl semimetal phases by introducing a nonreciprocal resistive coupling in the x-y plane that breaks time reversal symmetry. The first- and second-order Weyl points are connected by zero-admittance surface and hinge states, respectively. We also study the emergence of first- and second-order chiral modes induced by resistive couplings between similar nodes in the z direction. These modes, respectively, occur in the midgap of the surface and hinge admittance bands in our circuit model without the need for any external magnetic field.

DOI: 10.1103/PhysRevB.109.085430

I. INTRODUCTION

Topological materials can be classified as either gapped or gapless based on their energy-band spectra in momentum space [1–5]. The former hosts many exotic phenomena ranging from topological insulators [6,7], integer quantum Hall insulators [8–10], and topological superconductors [11,12] to higher-order topological insulators (HOTIs) [13,14]. These gapped topological phases are characterized by topological invariants such as the Chern number [15], Berry phase [16,17], and Z_2 invariant [18]. In contrast, gapless topological systems are characterized by the nature of their band-degeneracy points where two or more bands touch one another in momentum space. These band-degeneracy nodes are classified as either Dirac points (DPs) [19] or Weyl points (WPs) [20], depending on their symmetries. DPs emerge only when both time-reversal and inversion symmetries are present in a system. In contrast, WPs appear in the band dispersion if either or both symmetries are broken. Both types of band-touching points appear and annihilate pairwise. Two important classes of topological systems that host WPs and DPs are Weyl semimetals [3,21–24] and Dirac semimetals [25,26], respectively. In addition, it is worth noting that the energy-band dispersion can also feature a distinct type of band collapsing points, referred to as phenomenal points [27–29]. At these exceptional points, multiple eigenstates converge to a single, nonzero eigenenergy value, resulting in remarkable phenomena such as robust localized spectra and the restoration of biorthogonality among the eigenstates of a non-Hermitian system.

Recently, a class of three-dimensional (3D) topological phases named higher-order topological insulators, which go beyond the usual bulk-boundary correspondence, has been discovered [13]. In general, a d-dimensional nth-order topological insulator can host topologically protected $(d\text{-}n)$-dimensional gapless boundary states [30–32]. HOTIs are insulating in the bulk or surfaces and become metallic only when edges or hinges are introduced, respectively. They present intriguing multidimensional topological phenomena ranging from corner states to hinge states [13,14,33,34]. Interestingly, such unconventional nontrivial boundary modes are robust against system disorders and are protected by certain crystalline symmetries (e.g., reflection and mirror symmetries). Meanwhile, Weyl and Dirac semimetals have isolated band-touching points and exhibit unconventional properties such as the chiral anomaly and, in particular, Fermi arcs [35–38]. However, owing to the difficulties involved in finding suitable materials and the complexity in tuning model parameters, only a few experimental realizations of higher-order Weyl semimetals (HOWSMs) [39,40] and Dirac semimetals (HODSMs) [40] have been reported so far in acoustic crystal systems [41–43]. Interestingly, other higher-order nontrivial topological phases with unconventional topological band structures have been proposed in a multitude of platforms, e.g., in photonic [44,45], mechanical [46], and acoustic [47] systems, and in ultracold atomic gases in optical lattices [48,49], polaritons [50,51], microcavities [52], optical waveguides and fibers [44,53], non-Hermitian systems [54–56], and others [57]. Each of these platforms comes with experimental complexities and drawbacks, which makes them vulnerable to perturbations and nonuniformities.

In the search for alternative platforms to serve as experimental test beds for investigating topological states, lattice arrays with lossless electrical components such as inductors and capacitors known as topolectrical (TE) circuits have emerged as a frontrunner [23,27,29,58–72], as they offer better ability for tuning and modulating the system parameters. Because TE circuits are not constrained by physical dimensionality but rely solely on the mutual connectivities between the voltage nodes, HOTIs and higher-order gapless systems [39,40,73,74] (i.e., HODSMs and HOWSMs) can be readily

*rafiul.islam@u.nus.edu
†elesiuz@nus.edu.sg
‡sahinhaydar@u.nus.edu
§elembaj@nus.edu.sg

implemented using conventional electrical components. The gapless points in HODSMs and HOWSMs are protected by crystal symmetries and the WPs are connected by higher-order hingelike Fermi arc states rather than conventional surface arc states [39]. This suggests that highly robust hinge states can be achieved on the TE platform.

In this paper, we propose TE circuit networks that host HOWSM and HODSM nontrivial states that can be switched on and tuned solely by the choice of circuit parameters. We first construct a prototypical 2D TE circuit model, which exhibits a 2D quadrupole phase. To realize the gapless HOWSM and HODSM phases, we then stack copies of the 2D circuit lying on the x-y plane on top of one another along the z direction and couple the adjacent layers diagonally via a common stacking capacitor C_z. The stacking capacitor has the effect of modifying the intra- and intercell hopping in the effective 2D Laplacian as well as introducing an additional k_z dependence. Because the 3D circuit still obeys time-reversal and inversion symmetry, the circuit hosts pairs of DPs with higher-order topology. These symmetries can be broken by introducing a non-reciprocal resistive coupling that connects the nodes within a unit cell diagonally on the x-y plane. The symmetry breaking results in the emergence of first- and second-order WPs connected by a zero-admittance flat band, similar to surface and hinge Fermi arcs [75,76], respectively. A tilting capacitor C_t that connects the same types of nodes along the z axis can be further introduced to give rise to a tilted admittance dispersion while retaining the higher-order topology. A signature of these higher-order topologies is the localization of the squared amplitude of the nodal voltages, which is the TE equivalent of the quantum mechanical particle density, along the hinges of a 3D system having a nanowire geometry, i.e., with open boundary conditions (OBCs) along two dimensions. Finally, the chiral symmetry of the circuit lattice can be broken by introducing loss (positive resistance) and gain (negative resistance) terms between the same type of nodes in adjacent layers. This will result in the emergence of midgap chiral surface and hinge states in the midgap of the admittance spectra. These chiral modes are resilient against system perturbations and disorders. Therefore, both first- and second-order chiral states can be induced in the proposed TE circuit without any external magnetic field. These higher-order topologically nontrivial chiral states may find many applications in fault tolerant quantum computing [77], robust signal multiplexing [78], and dissipationless interconnects [79].

II. RESULTS

A. Topolectrical model

To realize higher-order topological gapless states, we consider a 3D TE circuit consisting of inductors, capacitors, resistors, and operational amplifiers, as shown in Fig. 1. The TE circuit has a unit cell [indicated by the dashed box in Fig. 1(a)] consisting of four sublattice nodes denoted as 1, 2, 3, and 4. The intracell and intercell couplings on the x-y plane are given by the capacitances of C_1 and C_2, respectively. The coupling strength linking nodes 4-1-4 in the y direction has a negative sign, denoting the inductive nature of the coupling (i.e., $-|C_i| = (\omega^2 L_i)^{-1}$, where ω is the frequency of the driving alternating current in the circuit). Additionally, the resistive couplings between the diagonal nodes within a unit cell are nonreciprocal and direction dependent, and are given by iR_d ($-iR_d$) for the solid (dashed) lines [Fig. 1(a)], where the resistive couplings in capital letters (e.g., R_j) are related to the physical resistance r_j through $R_j = 1/(i\omega r_j)$. Note that the positive and negative resistive elements in a TE circuit correspond to loss and gain terms in quantum mechanics. The π-phase shift or change of sign in the resistive coupling can be achieved by using the impedance converter setup shown in Fig. 1(b). The combination of two identical resistors r_1 and an ideal operational amplifier with supply voltages V_{dd}^{+} and V_{dd}^{-} effectively changes the resistance between nodes P and Q from r_a to $-r_a$, thus behaving as a negative resistance converter with a resistive coupling of $-iR_a$ (see Appendix A 1 for more details). These nonreciprocal loss (iR_d) and gain ($-iR_d$) terms are crucial in breaking the time reversal symmetry of the circuit to allow the system to host higher-order WPs, as will be discussed later.

To induce the higher-order gapless states with richer topological properties compared to their first-order counterparts, it is necessary to extend the TE circuit vertically in the z direction by stacking the two-dimensional (2D) x-y layers of the circuit shown in Fig. 1(a). The nodes in the unit cell are coupled diagonally in the x-z plane to the adjacent layer by a common capacitor C_z [see Fig. 1(c)]. The diagonal couplings within a unit cell on the y-z plane, which are of strength $-C_z$, are provided by an inductor [see Fig. 1(d)]. These interlayer couplings of $\pm C_z$ effectively modify the intracell couplings of the original admittance matrix of the 2D x-y circuit layer from $C_1 \to C_1 + 2C_z \cos k_z$ if we regard the vertical wave vector k_z as a model parameter. This modification translates the circuit Laplacian into a mathematically equivalent 2D SSH model, as will be discussed later. Additionally, the same types of nodes are connected to the adjacent vertical layers by a common tilting capacitance C_t. Aside from the interlayer capacitive and inductive couplings, there are also resistive ones. Nodes 1 and 4 (nodes 2 and 3) are connected to the corresponding nodes in the upper adjacent layer by a positive (negative) resistive coupling iR_c ($-iR_c$), respectively. These resistive couplings adopt the opposite sign when coupling to the lower adjacent layer [see Figs. 1(c) and 1(d)]. Finally, all the electrical nodes are connected to ground by a common inductor L and capacitor C [see Fig. 1(e)]. The capacitance C plays the role of the eigenenergy analogous to the Schrödinger equation [23,61,63], while the common inductance L allows tuning of the resonant frequency of the circuit. The other capacitors and resistors connecting each node to the ground [see Fig. 1(e)] ensure that the diagonal elements in the Laplacian matrix have the desired form as presented later in Eq. (1) [23].

The TE circuit depicted in Fig. 1 can be described in reciprocal space by the four-band circuit Laplacian,

$$\begin{aligned} Y(\omega, \boldsymbol{k}) = {} & i\omega((C_1 + C_2 \cos k_x)\sigma_x \otimes \sigma_0 + C_2 \sin k_x \sigma_y \otimes \sigma_z + (C_1 + C_2 \cos k_y)\sigma_y \otimes \sigma_y) \\ & + (C_2 \sin k_y \sigma_y \otimes \sigma_x + iR_1\gamma_1 - (2(C_1 + C_2) - (\omega^2 L)^{-1})\sigma_0 \otimes \sigma_0) + Y_z(k_z, \omega), \end{aligned} \tag{1}$$

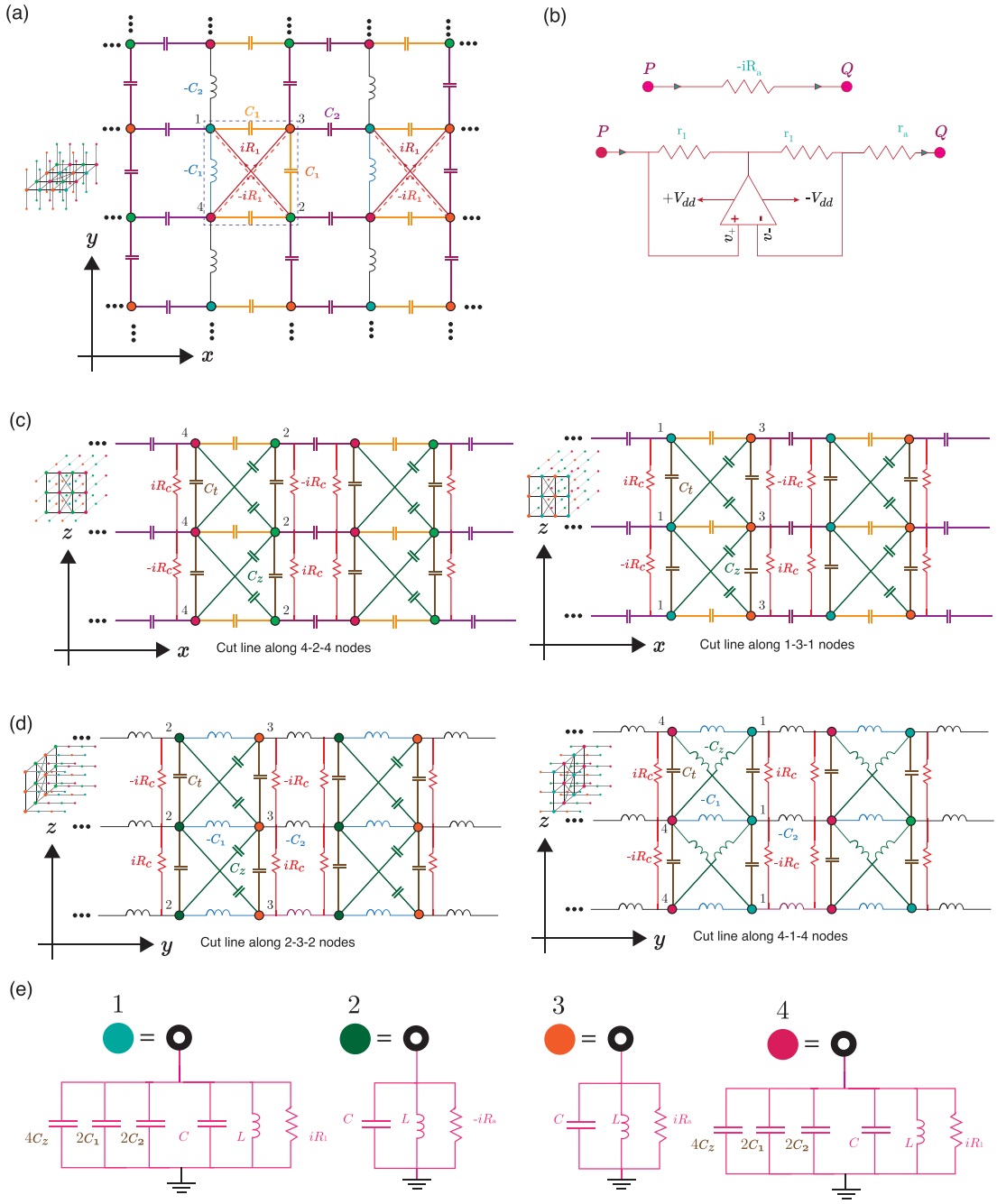

FIG. 1. Schematic of a TE circuit hosting higher-order semimetal states. (a) Cross section of the TE lattice model on the x-y plane. The blue, green, orange, and magenta circles represent the 1, 2, 3, and 4 sublattice sites or nodes, respectively. The dashed rectangle delineates a unit cell. The cartoon at the left of the lattice model schematically illustrates the crystal plane depicted. The intracell and intercell couplings along the x and y axes are given by capacitors C_1 and C_2, respectively. Note that there is an additional π-phase shift in the coupling linking the 4-1-4 nodes along the y axis compared to that linking the 2-3-2 nodes. The negative capacitance represents a frequency-dependent inductance (i.e., $-C_i = (\omega^2 L_i)^{-1}$). Nonreciprocal resistive couplings $\pm iR_d$ link diagonal nodes within the unit cell, giving rise to the breaking of time-reversal symmetry which is a requirement in realizing the Weyl-semimetal phase. (b) Negative impedance converter for providing an extra phase shift of π (change of sign) to the impedance and therefore converting a lossy resistive term R_a to a gain term $-R_a$. (c) Cross section of the TE lattice model on the x-z plane with the cut line at two different positions. The circuit is extended along the vertical z direction by stacking layers of the circuit lattice on the x-y plane described in (a) using capacitors, inductors, and resistors. Nodes 2 and 4, which are diagonal to each other, are connected by a common capacitor C_z. (d) Cross section of the TE lattice model on the y-z plane with the cut line at two different positions. The diagonal nodes of the cut lines along the $4-1-4$ and $2-3-2$ nodes are connected by an inductor $-C_z$ and capacitor C_z, respectively. Note that, for (c) and (d), the same type of nodes are connected along z axis by a resistive element R_c with alternating signs and a tilting capacitance C_t. (e) Grounding mechanism of the TE circuit for all four types of nodes. The common grounding capacitor C serves the role of the eigenenergy while the common inductor L is added to make the momentum-independent diagonal elements in the Laplacian matrix zero, which is analogous to setting the on-site energy to zero for a condensed matter tight-binding Hamiltonian.

where $Y_z(\omega, k_z)$ is given by

$$\begin{aligned} Y_z(\omega, k_z) = & i\omega(2C_z \cos k_z(\sigma_x \otimes \sigma_0 + \sigma_y \otimes \sigma_y)) \\ & + (2R_c \sin k_z \sigma_z \otimes \sigma_z + 2C_t \cos k_z \sigma_0 \otimes \sigma_0 \\ & - 4C_z \sigma_0 \otimes \sigma_0), \end{aligned} \tag{2}$$

where σ_i denotes the ith Pauli matrices in the sublattice space, σ_0 is the 2×2 identity matrix, $\gamma_1 = (\sigma_y \otimes \sigma_x)$ $(\sigma_y \otimes \sigma_z)$, $C_i(-C_i)$ is the coupling capacitance (inductance), and R_1 and R_c are the resistive coupling strengths that break time-reversal and chiral symmetry, respectively. We set the resonant frequency in such a way that the **k**-independent coefficients of the identity matrix vanish (i.e., $\omega_r = 1/\sqrt{2L(C_1 + C_2 + 2C_z)}$). This is equivalent to setting the on-site energy to zero at each lattice site in a tight-binding Hamiltonian [80].

As we shall show in the remainder of this paper, in general, Eq. (1) describes a 3D Weyl semimetal system that hosts multiple band-touching WPs. Each of these WPs may be a first-order WP, at which the system switches between a first-order Chern insulator and a topologically trivial phase, or a second-order WP, in which the system switches between a first-order Chern insulator phase and a 2D second-order quadrupole topological insulator phase. For some parameter ranges, the system may contain a mixture of first- and second-order WPs and therefore present a hybrid phase where topologically trivial, and first and second-order 2D topological phases exist at different k_z values.

B. Higher order Dirac semimetals: $R_1 = 0, R_c = 0, C_t = 0$

In the absence of the resistive couplings and the tilting capacitance C_t and at resonant frequency, the TE circuit satisfies chiral, inversion, reflection (across all three of the x, y, and z axes) and mirror rotation symmetries. Mathematically, the circuit Laplacian in Eq. (1) satisfies the following:

$$\begin{aligned} \mathcal{C}Y(\omega_r, k_x, k_y, k_z)\mathcal{C}^{-1} &= -Y(\omega_r, k_x, k_y, k_z), \\ \mathcal{I}Y(\omega_r, k_x, k_y, k_z)\mathcal{I}^{-1} &= Y(\omega_r, -k_x, -k_y, -k_z), \\ \mathcal{T}Y(\omega_r, k_x, k_y, k_z)^*/(i\omega)\mathcal{T}^{-1} &= Y^\dagger(\omega_r, -k_x, -k_y, -k_z)/(i\omega), \\ \mathcal{M}_x Y(\omega_r, k_x, k_y, k_z)\mathcal{M}_x{}^\dagger &= Y(\omega_r, -k_x, k_y, k_z), \\ \mathcal{M}_y Y(\omega_r, k_x, k_y, k_z)\mathcal{M}_y{}^\dagger &= Y(\omega_r, k_x, -k_y, k_z), \\ \mathcal{M}_z Y(\omega_r, k_x, k_y, k_z)\mathcal{M}_z{}^\dagger &= Y(\omega_r, k_x, k_y, -k_z), \\ \mathcal{M}_{xy} Y(\omega_r, k_x, k_y, k_z)\mathcal{M}_{xy}{}^\dagger &= Y(\omega_r, k_y, k_x, k_z), \end{aligned} \tag{3}$$

where $\mathcal{C}$, $\mathcal{I}$, $\mathcal{T}$, $\mathcal{M}_i$, and $\mathcal{M}_{xy}$ are the chiral, inversion, time reversal, reflection about the ith axis with $i \in \{x, y, z\}$, and xy mirror-rotation (i.e., about the $\hat{x} + \hat{y}$ direction) operators, respectively.

In terms of the Pauli matrices, these operators are explicitly given by $\mathcal{C} = \sigma_z \otimes \sigma_0$, $\mathcal{I} = \sigma_0 \otimes \sigma_y$, $\mathcal{T} = \sigma_0 \otimes \sigma_0$, $\mathcal{M}_x = \sigma_x \otimes \sigma_z$, $\mathcal{M}_y = \sigma_x \otimes \sigma_x$, and $\mathcal{M}_z = \sigma_0 \otimes \sigma_0$.

In our subsequent analysis of the system, we will also occasionally find it useful to treat k_z as a tunable parameter rather than referring to a spatial dimension, i.e., we regard $Y(\omega_r, k_x, k_y, k_z)$ as describing a quasi-2D system in x and y indexed by the parameter k_z. In a TE context, this can always be realized by interpreting Eq. (1) as the Laplacian for a 2D circuit in which the $Y_z(\omega, k_z)$ term is now an on-site potential parameterized by the tunable parameter k_z, which is realized in the circuit by connecting capacitors, inductors, and resistors with the appropriate values at each voltage node to the ground.

Taking k_z as a parameter in this way, $Y(\omega_r, k_x, k_y, k_z)$ is also symmetric under the 2D particle–hole conjugation ($\mathcal{P}_{2D}$), time-reversal ($\mathcal{T}_{2D}$), and chirality C_{2D} operations,

$$\mathcal{P}_{2D} Y(\omega_r, k_x, k_y, k_z)^{\mathrm{tr}} \mathcal{P}_{2D}^{-1} = -Y(\omega_r, -k_x, -k_y, k_z), \tag{4}$$

$$\mathcal{T}_{2D} Y(\omega_r, k_x, k_y, k_z)^*/(i\omega)\mathcal{P}_{2D}^{-1} = Y(\omega_r, -k_x, -k_y, k_z)/(i\omega), \tag{5}$$

$$C_{2D} Y(\omega_r, k_x, k_y, k_z)^{\mathrm{tr}} C_{2D}^{-1} = -Y(\omega_r, -k_x, -k_y, k_z), \tag{6}$$

where $\mathcal{P}_{2D} = \sigma_x \otimes \sigma_0$, and $\mathcal{T}_{2D}$ and C_{2D} have the same forms as $\mathcal{T}$ and C, respectively. The quasi-2D system hence belongs to the BDI Altland-Zimbauer (AZ) class [81], for which the first-order topological states are not characterized by any topological invariant.

In the absence of the resistive couplings and tilting capacitance C_t, the admittance eigenvalues of Eq. (1) for the bulk periodic system take the form of

$$\begin{aligned} &\mathcal{J}(\omega, k_x, k_y, k_z) \\ &= \pm\omega \sqrt{\sum_{i=x,y} ((C_1 + 2C_z \cos k_z + C_2 \cos k_i)^2 + (C_2 \sin k_i)^2)}. \end{aligned} \tag{7}$$

The admittance band gap closes at $(k_x, k_y, k_z) = (0, 0, \kappa_z{}^{D1})$ and $(k_x, k_y, k_z) = (0, 0, \kappa_z{}^{D2})$, where $\kappa_z{}^{D1} = \pm\cos^{-1}\left(-\frac{C_1+C_2}{2C_z}\right)$ and $\kappa_z{}^{D2} = \pm\cos^{-1}\left(-\frac{C_2-C_1}{2C_z}\right)$. We consider the first case where the bands touch at κ_z^{D1} (a similar behavior occurs for the other case where band gap closing occurs at κ_z^{D2}). If $|C_1 + C_2| < |2C_z|$, the inversion and time-reversal symmetries guarantee the existence of pair of twofold degenerate DPs in k space for the bulk admittance band structure [see Fig. 2(a)]. The imposition of a finite width, i.e., OBCs, on this system along the x direction while retaining periodic boundary conditions (PBCs) along the y and z directions results in a nanoplate geometry. Surface edge states localized near the x boundaries of the nanoplate now emerge and connect the pair of DPs [see Fig. 2(b)]. These midgap edge modes are Fermi arc states that connect two gapless points with opposite topological charges in conventional (first-order) Weyl semimetals [22,23].

Next, we now further impose a finite width on the y direction so that a nanowire geometry with OBCs in the x and y directions and PBCs in the z direction is formed. The Fermi arc states in the nanoplate geometry now become quantized into subbands because of the geometrical confinement along the y direction and no longer cross the gap [Fig. 2(c)]. A nearly flat state linking the two DPs appears in the admittance dispersion along the k_z axis [see Fig. 2(c)]. This state is a higher-order state because it emerges only when the system is confined along two directions. Figure 2(d) shows that this state is indeed a hinge state, using the example of the $k_z = 0$ states—the square of the voltage amplitude (the analog of the probability density) is localized along the corners of the nanowire cross section.

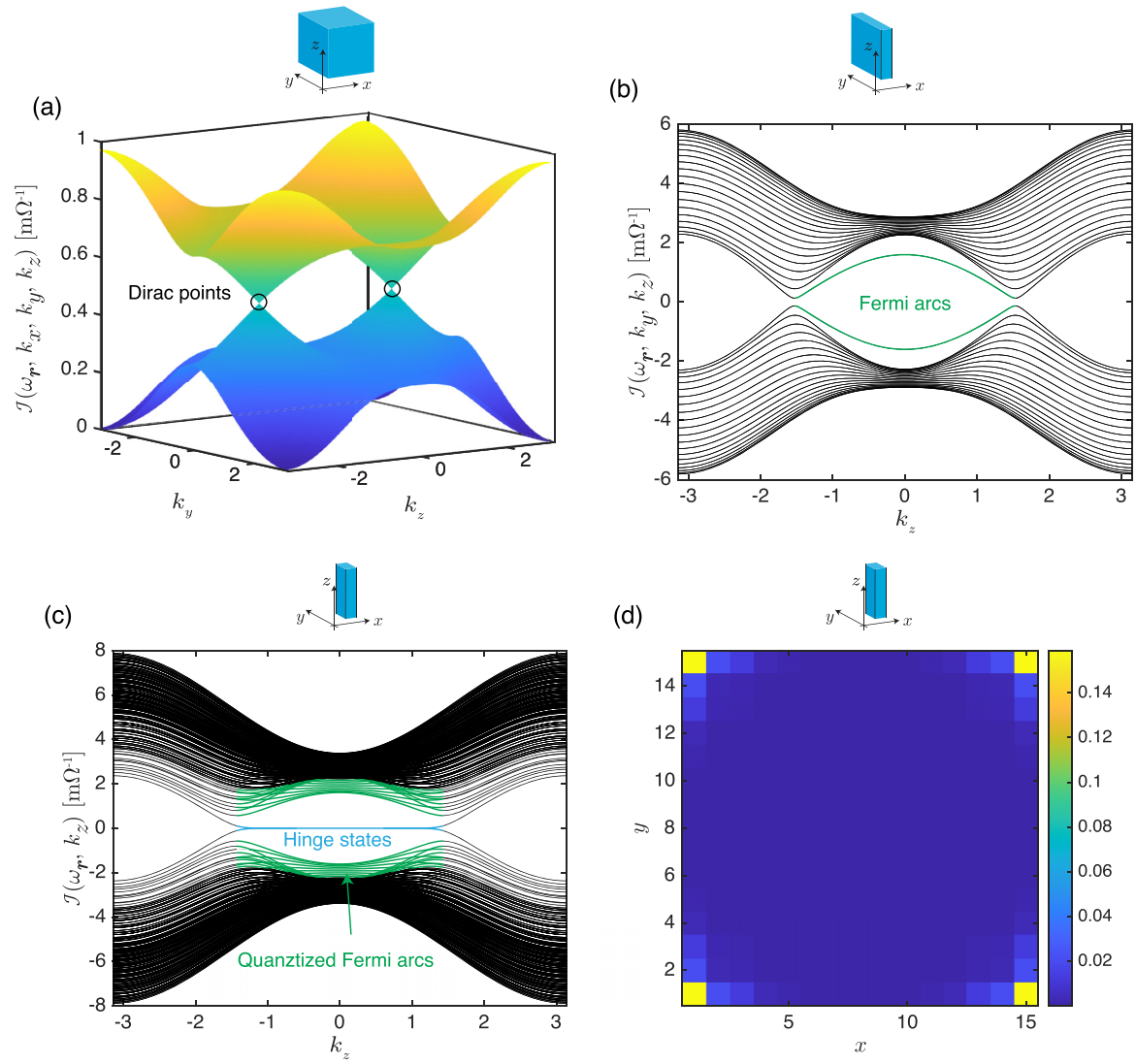

FIG. 2. (a) Admittance dispersion relation for the infinite (bulk) TE circuit model described in Eq. (1) at $k_x = 0$. Clearly, there exists a pair of Dirac points on the k_y axis. (b) Admittance spectrum of the TE circuit in a nanoplate geometry consisting of 15 unit cells in the finite x direction and PBC in the infinite y and z directions with $k_y = 0$. Note the two Fermi arc edge states connecting the Dirac points. (c) The admittance dispersion of the TE circuit in the nanowire geometry with PBCs along the z direction and OBCs in both the x and y directions. Note the flat-band hinge state connecting two Dirac points. (d) Squared nodal voltage amplitude distribution of the $k_z = 0$ hinge state in the nanowire geometry. Only the nodes at the corner exhibit significant voltages, indicating the presence of topological conducting hinge states. The cartoon on top of each panel indicates the confinement geometry (bulk, or confinement along one or two directions) considered in the respective panel. The common parameters are $C_1 = -2$ mF, $C_2 = 2$ mF, $C_z = 0.8$ mF, $R_c = 0$, and $C_t = 0$.

Because the Laplacian obeys both chiral C and mirror rotational symmetries $\mathcal{M}_{xy}$ [see Eqs. (3)], the Laplacian can be transformed via a unitary transform into a block diagonal form along the $k_x = k_y = k$ high-symmetry line [13,33]. The transformed Laplacian is given by

$$\chi^{-1} Y(\omega_r, k, k_z)\chi = \begin{bmatrix} Y_1(\omega_r, k, k_z) & 0 \\ 0 & Y_2(\omega_r, k, k_z) \end{bmatrix}, \quad (8)$$

where χ is a unitary transformation. The diagonal elements of the transformed block matrix [45] can be expressed as

$$Y_{1,2}(\omega_r, k, k_z) = (C_1 + 2C_z \cos k_z + C_2 \cos k)\sigma_x + \eta_{1,2} C_2 \sin k \sigma_y, \quad (9)$$

where, $\eta_{1,2} = 1$ (-1) for Y_1 (Y_2), respectively. [The fact that the matrix in Eq. (8) is related to $Y(\omega_r, k, k_z)$ via a unitary transform can be verified by noting that they share the same set of eigenvalues.] Interestingly, Eq. (9) represents a modified SSH model with a k_z-dependent intracell coupling. Therefore, the resultant (4×4) admittance matrix in Eq. (8) can be regarded as two decoupled SSH blocks. If we consider k_z as a model parameter, the winding number ($\mathcal{W}$) of the TE circuit, which serves as its topological index, can be obtained (see Appendix for details) as

$$\mathcal{W} = \begin{cases} 2, & \text{if } \left|\frac{C_1 + 2C_z \cos k_z}{C_2}\right| \leqslant 1 \\ 0, & \text{otherwise.} \end{cases} \quad (10)$$

The above results thus show that the parameter regime with flat hinge states connecting the two DPs in Fig. 2(c) carries a topological index of two, confirming its character as a higher-order hinge Fermi arc. We can thus classify the circuit as a HODSM.

C. Higher-order chiral hinge states in higher order topological circuit array: $R_1 = 0, R_c \neq 0, C_t = 0$

In the previous section, we discussed the evolution of HODSM phases in a LC circuit lattice. In this subsection, we will study the effect of resistive coupling along the z direction [in the form of a finite R_c in Eq. (1)] on the higher-order topology of the circuit model. A nonzero R_c in Eq. (1) corresponds to alternating iR_c and $-iR_c$ couplings between adjacent layers of the circuit along the z direction, as shown in Figs. 1(b) and 1(c).

A finite R_c breaks the reflection symmetry in the x and z directions, as well as the chiral symmetry. However, it preserves inversion symmetry, as well as the reflection symmetry in the y direction. Treating the system as a quasi-2D system, where k_z is regarded as a tunable parameter rather than a spatial dimension, R_c breaks the symmetry of the system under the 2D particle-hole conjugation $\mathcal{P}_{2D}$ and chirality C_{2D} operatons. The quasi-2D system hence belongs to the AI Altlad-Zimbauer class, for which there is no first-order topological invariant.

The finite R_c also breaks the degeneracy of the bulk admittance dispersion such that the two pairs of twofold degenerate bands in the admittance spectrum split into four nonoverlapping bands, as shown in Fig. 3(a). (The presence of four bands can be seen from the fact that there are two separate sheets below the bulk band gap and two separate sheets above the band gap.) Compared to the zero-R_c scenario shown in Fig. 2, where the doubly degenerate band-touching DPs exist at only two distinct points in k space that lie on the $k_y = 0$ line, the finite R_c results in the emergence of bulk WPs at four distinct points in k space that are displaced away from $k_y = 0$.

These WPs demarcate the k_y boundaries of the k-space region where band-touching points due to midgap states exist when a finite width is introduced along the x direction to form a nanoplate, as shown in Fig. 3(b). Figure 3(b) shows the projection of the bulk WPs on the k_y–k_z plane (the four circles) and the (logarithm of the) band gap where the dark blue arc corresponding to very small magnitudes of the band gap indicates the band-touching points of the midgap surface states. Figure 3(c) shows an exemplary dispersion relation for the nanoplate at the specific value of $k_y = 0$, which is denoted by the black dotted line in Fig. 3(b). Four distinct midgap Fermi arc surface states are clearly evident in the dispersion relation.

Finally, when OBCs are imposed in both the x and y directions and PBCs in the z direction to form a nanowire geometry, a pair of chiral hinge states that crosses at $k_z = 0$ and closes the gap emerges. In both Figs. 2 and 3, where $R_1 = R_c = 0$, the preservation of time-reversal symmetry results in a net Chern number of zero calculated by treating k_z as a tunable parameter at all k_z values in the system despite the presence of surface states in the nanoplate geometry. (More details on the Chern number are provided in the Appendix A 2.) The higher-order hinge states in both Figs. 2(c) and 3(d) can also be characterized by the quantized quadrupole moment index by treating the system as a quasi-2D system parameterized by k_z. In this case, the quadropole index has a finite value only when the Chern number is 0 [39,82]. The absence of a finite Chern number at all k points when $R_1 = R_c = 0$ allows the higher-order hinge states to coexist within the same k_z ranges as the first-order surface states, unlike the examples with a finite Chern number due to broken time-reversal symmetry that we study later.

D. Tilted chiral hingestates : $R_1 = 0, R_c \neq 0, C_t \neq 0$

We consider the effects of tilting on the admittance band dispersion. As can be seen from Eq. (1), a finite value of C_t leads to a tilt in the dispersion. In Fig. 4, we plot the admittance spectra as a function of k_z for nonzero C_t. The presence of tilt leads to a drastic modification of the edge and chiral hinge states. Interestingly, the edge states survive even when the whole spectra becomes overtilted when we consider a TE system with OBCs in the x direction and PBCs in the y and z directions [whose dispersion is shown in Fig. 4(a)]. However, both edge states acquire the same sign of the admittance slope in the vicinity of each DP.

The chiral hinge modes that emerge when OBCs are imposed on both the x and y directions show some peculiar characteristics [see Fig. 4(b)]. The two chiral hinge states propagate in a direction that is valley dependent. At $k_z = 0$, both chiral hinge modes have zero group velocity, but at finite values of $|k_z|$, they exhibit the same sign of the admittance slopes, as shown in Fig. 4(b). In other words, the hinge states in the K (K') valley propagate with positive (negative) group velocities in the z direction. These overtilted higher-order edge and hinge states can be termed as type-2 topological states [61] and show a sharp contrast to the type-1 surface and hinge states where both the K and K' valleys host states with both positive and negative group velocities.

E. Higher-order chiral Weyl semimetals: $R_1 \neq 0, R_c \neq 0, C_t = 0$

We will now construct a TE circuit model that hosts Chern insulator states by breaking time-reversal symmetry through the incorporation of finite nonreciprocal (R_1) resistive couplings into the circuit. From Eq. (1), we obtain the k_z-dependent admittance dispersion at ($k_x = k_y = 0$) as

$$\mathcal{J}(\omega, k_z) = \pm\omega R_1 \pm \omega\sqrt{2\big((C_1 + C_2)^2 + 2C_z^2 + R_c^2 + 4(C_1 + C_2)C_z \cos k_z + \big(2C_z^2 - R_c^2\big)\cos(2k_z)\big)}. \tag{11}$$

A finite R_1 breaks the time-reversal, M_x, and M_y symmetries while preserving the M_y and inversion symmetries. Treating k_z as a parameter rather than a spatial dimension, R_1 preserves the symmetry of the system under 2D particle–hole

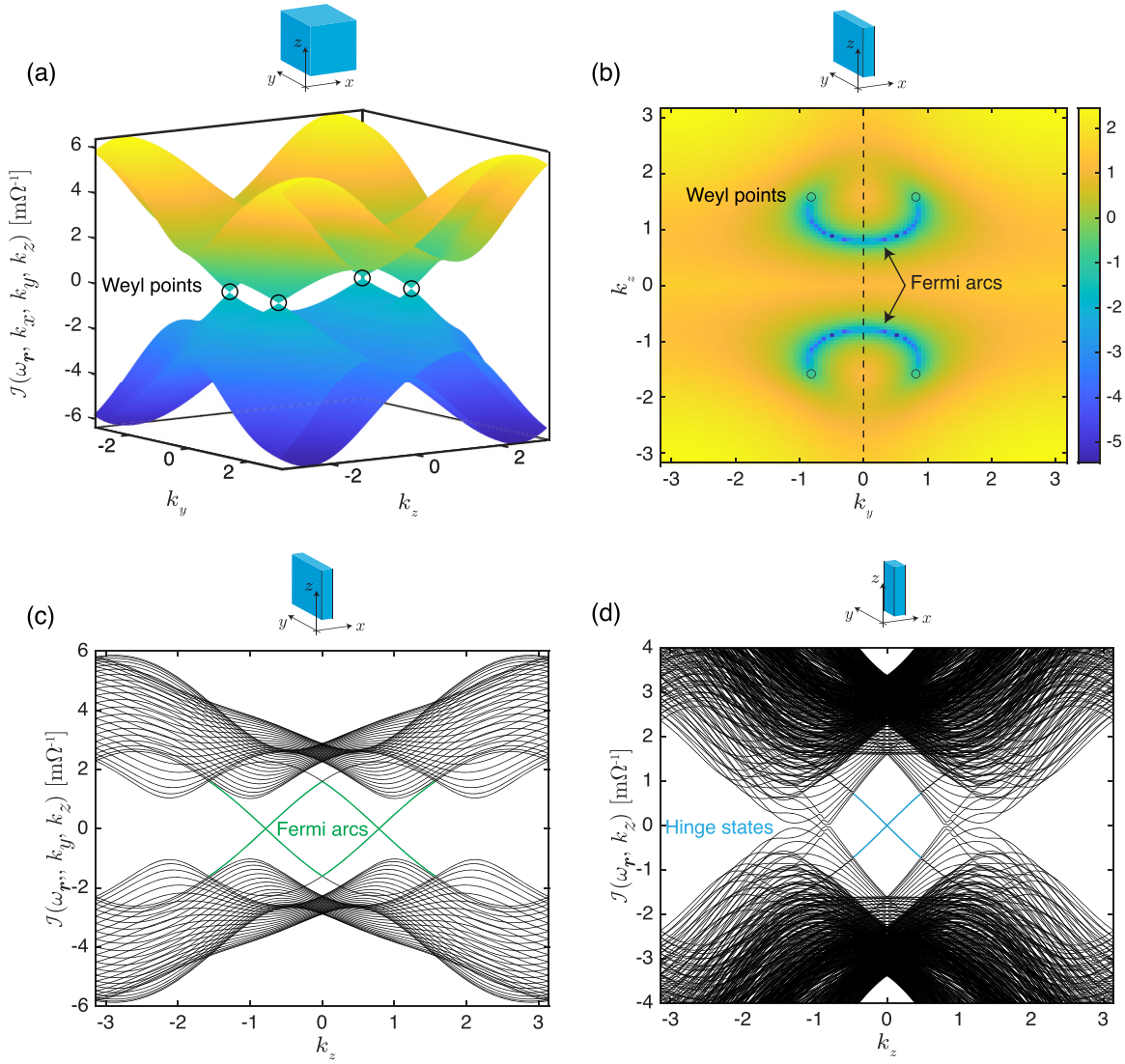

FIG. 3. (a) Bulk admittance band dispersion for the TE model described in Eq. (1) with finite R_c at $k_x = 0$. A nonzero value of R_c displaces the Weyl points away from the k_y axis. (b) Logarithm of the band gap in a nanoplate geometry with 15 unit cells along the x direction and PBCs along the y and z directions. The dark blue arcs with large negative values correspond to the band-touching points of the Fermi arcs on the k_y-k_z plane. The Fermi arcs terminate at the k_y-k_z plane projections of the bulk Weyl points, which are denoted as circles. The black dotted line indicates $k_y = 0$, at which the admittance spectrum in (c) is plotted. (c) Admittance spectrum of a circuit in (b) at $k_y = 0$. (d) Chiral topological hinge states appear when OBCs are imposed in both the x and y directions. The common parameters are $C_1 = -2$ mF, $C_2 = 2$ mF, $C_z = 0.8$ mF, $R_c = 0.8$ mF, and $C_t = 0$.

conjugation $\mathcal{P}_{2D}$ but breaks chiral symmetry under C_{2D}. The quasi-2D system hence belongs to the D AZ class. When a finite R_c is further imposed on the system on top of the finite R_1, the inversion and conjugation symmetries are broken as well, and the quasi-2D system belongs to the A AZ class. The first-order topology of both the A and D AZ classes can be characterized by the Chern number.

The broken TRS symmetry due to R_1 allows for the emergence of WPs that demarcate the boundaries between first-order topologically nontrivial Chern insulator phases and either the topologically trivial phase or the 2D quadruopole insulator phase. When $R_1 \neq 0$, the system hosts a pair of WPs at $(0, 0, k_z^{\text{Weyl}})$, where k_z^{Weyl} is the resistive element-dependent position of the WPs on the k_z axis and is given by

$$k_z = \pm\cos^{-1}\left(-\frac{(C_1+C_2)C_z}{2C_z^2-R_c^2} \pm\frac{1}{2}\frac{2C_z^2R_1^2+R_c^2(2C_1+C_2)^2-8C_z^2-R_1^2+4R_c^2)}{\left(2C_z^2-R_c^2\right)^2}\right). \tag{12}$$

To explain the role of the nonreciprocal resistive element R_1 on the behavior of the WP, we can further simplify Eq. (12) by considering the case where $R_c = 0$,

$$k_z = \pm\cos^{-1}\left(-\frac{2(C_1+C_2)+\eta\sqrt{2}R_1}{4C_z}\right), \tag{13}$$

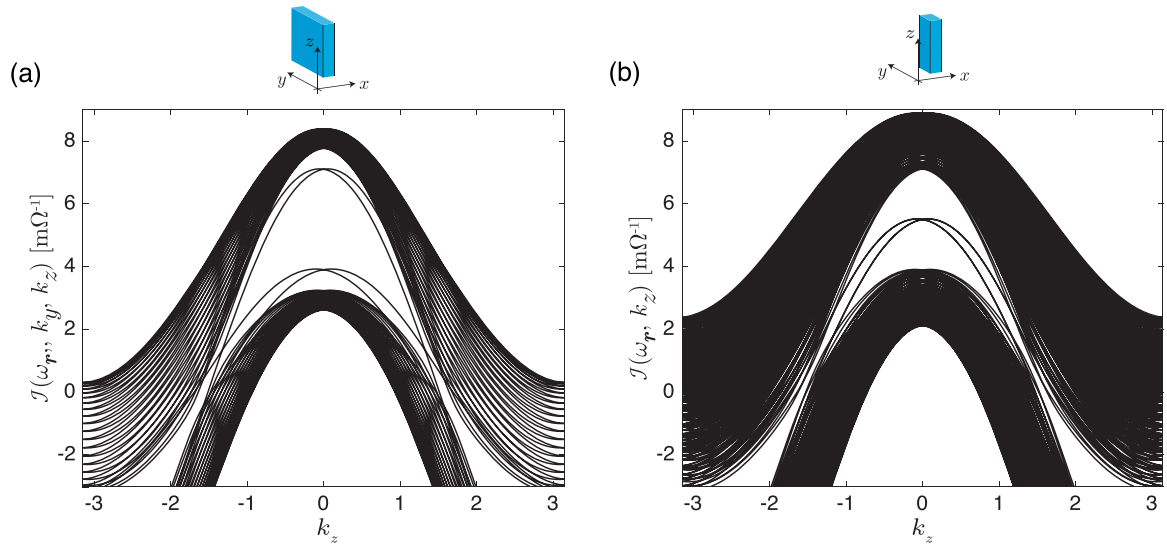

FIG. 4. Type-2 chiral modes in TE model with a finite tilting capacitance C_t. (a) Surface admittance spectra for a TE circuit with OBCs in the x direction with 15 unit cells, and PBCs in the y and z directions at $k_y = 0$. (b) Admittance dispersion exhibiting type-2 hinge modes in a TE circuit with OBCs in both the x and y directions (with 15 unit cells along both these directions). Note that the two chiral hinge states propagate in a valley-dependent direction, i.e., they exhibit only positive (negative) group velocity in the z direction at the K (K') valley. The common parameters are $C_1 = -2$ mF, $C_2 = 2$ mF, $C_z = 0.8$ mF, $R_c = 0.2$ mF, $R_1 = 0$ mF, and $C_t = 2.75$ mF.

where η can take the values of ± 1. The two possible values for η correspond to two different types of WPs with distinct Fermi arc behavior, which we refer to as first-order and second-order WPs for reasons that will become apparent shortly. Depending on whether real solutions for k_z exist for only $\eta = 1$, only $\eta = -1$, or both $\eta = \pm 1$, we will obtain pairs of only first-order WPs, only second-order WPs, or both types of WPs, respectively.

We first consider the case where Eq. (13) has real solutions only for $\eta = +1$. Figure 5(a) shows the dispersion relation for an exemplary set of parameters for which this condition holds in a nanoplate geometry with OBCs along the x direction and PBCs along the y and z directions at $k_y = 0$. A pair of midgap surface states with a nearly flat dispersion crosses the band gap at large values of $|k_z|$. Figure 5(b) shows (the logarithm of) the band gap magnitude on the k_y–k_z plane and the projections of the two bulk WPs. The dark blue regions lying on the k_y axis, which represent very small magnitudes of band gap, correspond to the minimum energy difference between the hole- and particlelike surface states. In particular, the hole- and particlelike surface states touch along a certain pair of $\pm k_z$ values lying on the k_y axis, where the band gap tends towards 0. The k_z values of the projections of the bulk WPs, which are denoted by the horizontal dotted lines, demarcate the boundaries of the regions at which the surface states exist. These bulk WPs are band-touching points at which the system undergoes topological phase transitions between the first-order topologically nontrivial phase with a finite Chern number and midgap states, and either the topologically trivial phase, at which no midgap states exist, or the second-order quadrupole TI phase, at which midgap states exist only in the nanowire geometry but not the nanoplate geometry. The WPs in Fig. 5 are first-order WPs because they mark transitions between the first-order topological and topologically trivial phases. The absence of second-order midgap states in this system can be seen from the absence of midgap hinge states that cross the band gap in the nanoplate geometry [Fig. 5(c)] and the large magnitude of the band gap in Fig. 5(d).

We now consider the effects of setting R_c to a finite value for the same parameter settings as in Figs. 5(a)–5(d). Figure 5(e) shows the admittance relation in the nanoplate geometry at $k_y = 0$. Similar to the $R_c = 0$ case, a pair of surface states is present at large $|k_z|$ values. Compared to the $R_c = 0$ case, the surface states in the finite R_c case evidently have a larger k_z dispersion, and the minimum energy difference between the hole- and particlelike states shown in this plot occurs at $k_z = \pm\pi$. From the plot of the logarithm of the band-gap magnitude across the entire k_y–k_z plane in Fig. 5(f), it can be seen that these trends can be attributed to the shifting of the minimum energies of the midgap surface states away from the k_y axis (except at $k_z = \pm\pi$) induced by the finite R_c. In particular, the zero-energy states where the hole- and particlelike surface states touch do not lie on the $k_y = 0$ line, but rather at a pair of $\pm|k_y|$ values with finite magnitudes. Figure 5(f) also shows that, although the bulk WPs are displaced away from the $k_y = 0$ line by the finite R_c, the k_z values of the bulk WPs still demarcate the boundaries of the k_z ranges at which surface states exist. Figures 5(g) and 5(h) show that second-order hinge states are still absent in the nanowire geometry even after the introduction of a finite R_c.

In comparison, Fig. 6 shows the counterpart to Fig. 5 for a parameter set where Eq. (13) has solutions only for $\eta = -1$ at $R_c = 0$. Similar to Figs. 5(a) and 5(b), Figs. 6(a) and 6(b) show that first-order surface states exist in a nanoplate geometry within a k_z region bounded by the projections of the bulk WPs. The k_z range that hosts the surface states corresponds to that in which the Chern number has a finite value, while the k_z values of the bulk WPs are those where phase transitions between topological phases with 0 and finite Chern numbers occur when the bulk band gap closes at the WPs. In contrast

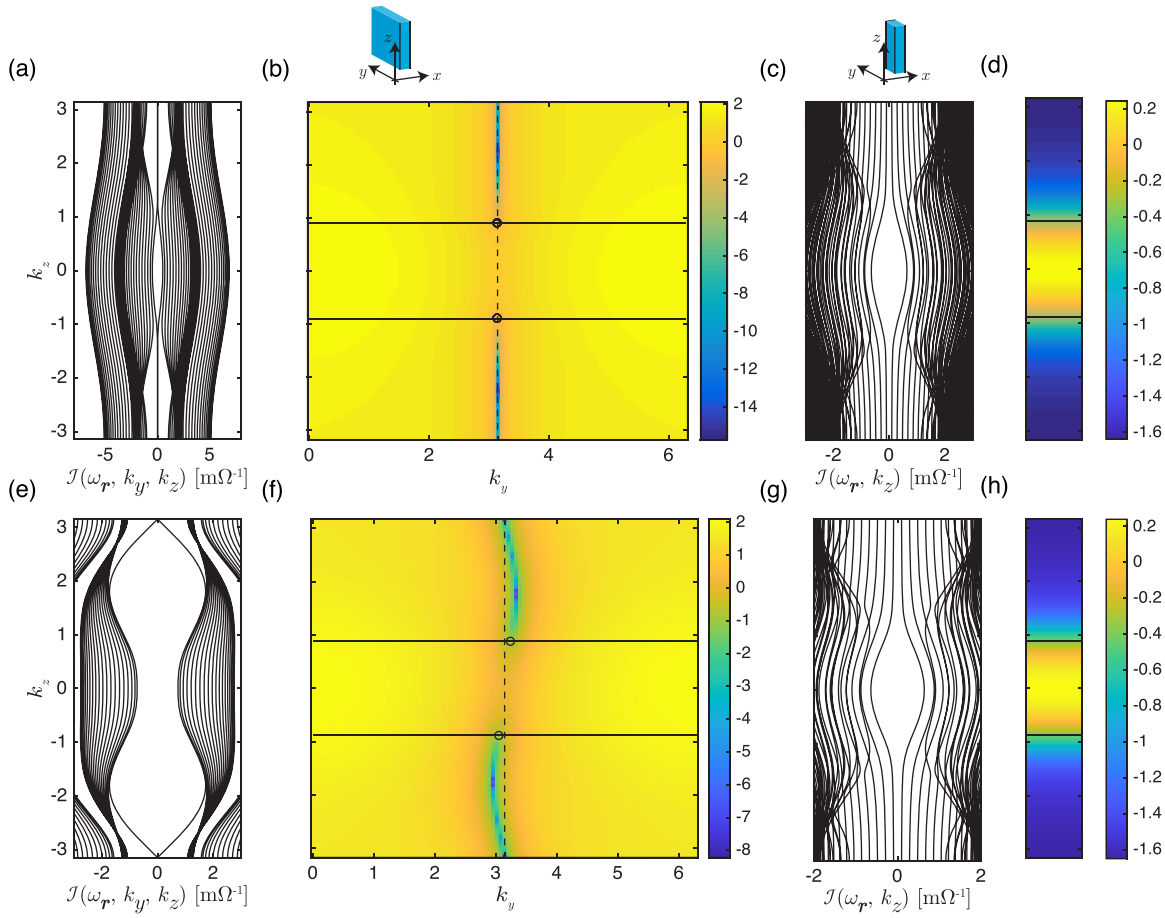

FIG. 5. Evolution of the admittance band structure of the circuit model in Eq. (1) with nonzero resistive elements when only $\eta = +1$ solutions exist for Eq. (13). (a) Admittance spectrum of a TE circuit exhibiting only first-order chiral states with a finite R_1 and zero R_c with 15 unit cells along the x direction and PBCs along the y and z directions at $k_y = 0$. The presence of gap-crossing surface states is evident at large $|k_z|$ values. (b) The logarithm of the band gap on the k_z–k_y plane for the system in (a). The two black circles denote the projections of the bulk Weyl points on the k_z–k_y plane. The k_z values of these points demarcate the boundaries at which surface states, which correspond to the dark blue areas, indicating small values of band gaps, exist in the nanoplate geometry. The vertical black dotted line denotes the $k_y = 0$ line that (a) is plotted for. (c), (d). The (c) admittance spectrum and (d) logarithm of the band gap for the system in (a) in a nanowire geometry with OBCs along the x and y directions and PBCs along the z direction. The horizontal black lines in (c) and (d) denote the k_z values of the bulk Weyl points. No chiral hinge states emerge in the admittance spectrum in (c), which is further corroborated by the relatively large magnitude of the band gap for all values of k_z. (e)–(h) are the counterparts of (a)–(d) for a system with the same parameters as (a)–(d) except that R_c now has a finite value of 0.2 mF. The common parameters are $C_1 = -1$ mF, $C_2 = 2$ mF, $C_z = 0.4$ mF, $R_1 = 1.414$ mF, and $C_t = 0$ mF.

to Figs. 5(c) and 5(d), Figs. 6(c) and 6(d) show that the bulk WPs at $\eta = -1$ are marked by the emergence of second-order chiral hinge states that cross the bulk band gap [the fact that these hinge states cross the bulk gap can be seen from Fig. 6(d), where the logarithm of the band gap approaches $-\infty$ at $k_z = 0$]. These hinge states occur in the k_z ranges where the Chern number is zero and there are no first-order surface states. These WPs are therefore second-order WPs. Figures 6(e)–6(g) show the counterparts to Figs. 6(a)–6(d) when a finite R_c of 0.2 is applied. Similar to its effects in Figs. 5(e) and 5(f), the R_c displaces the minimum energies of the surface states and their band-touching points away from the k_y axis. This results in the surface states having a larger $_z$ dispersion in Fig. 6(e) and the minimum energy separation between the hole- and particlelike surface states occurring away from $k_y = 0$ in Fig. 6(f). Figures 6(g) and 6(h) show that the higher-order chiral hinge states that emerge in the nanowire geometry are still present even when a finite R_c is introduced.

The systems in Figs. 5 and 6 serve as specific examples that band-gap closing at the bulk WPs leads to phase transitions between topological phases with and without a finite Chern number. In these systems with broken time-reversal symmetry due to a finite R_1, the topological phases with finite Chern numbers host first-order topological surface states but no second-order hinge states. The phases with a Chern number of 0 may either be topologically trivial and host no first- or second-order topological zero modes (e.g., the small $|k_z|$ region in Fig. 5), or have a finite QTI index and host second-order hinge states but no first-order surface states (e.g., the small $|k_z|$ region in Fig. 6). Besides the WPs at various values of k_z and $k_x = k_y = 0$ considered earlier, WPs may also exist at $k_x, k_y = \pm\pi$ depending on the values of C_1, C_2, C_z, and R_1 when $R_c = C_t = 0$. This implies that the system

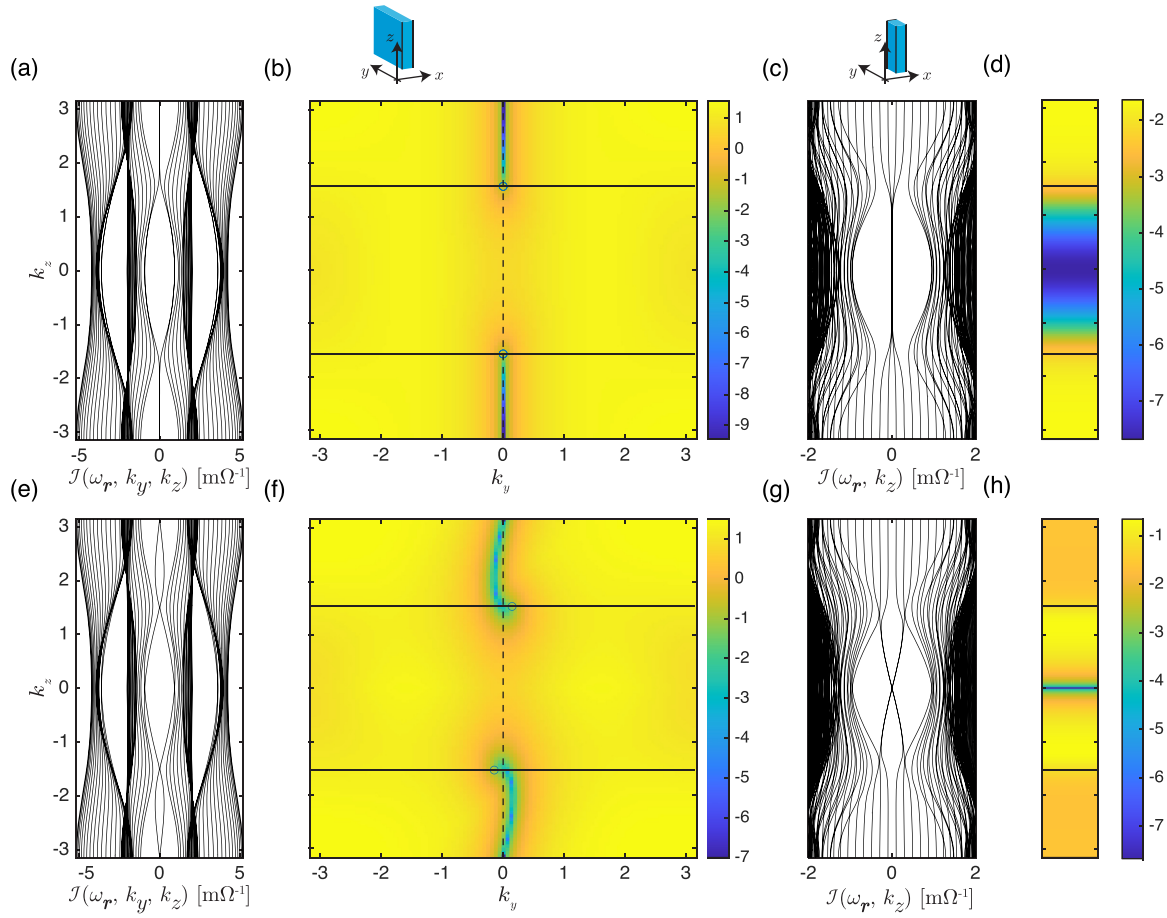

FIG. 6. Evolution of the admittance band structure of the circuit model in Eq. (1) with nonzero resistive elements when only $\eta = -1$ solutions exist for Eq. (13). (a) Admittance spectrum of a TE circuit with a finite R_1 and zero R_c with 15 unit cells along the x direction and PBCs along the y and z directions at $k_y = 0$. The presence of midgap surface states is evident at large $|k_z|$ values. (b) The logarithm of the magnitude of the band gap on the k_z–k_y plane for the system in (a). The two black circles denote the projections of the bulk band-touching Weyl points on the k_z–k_y plane. The k_z values of these points demarcate the boundaries at which surface states, which correspond to the dark blue areas with small values of band gaps, exist in the nanoplate geometry. The vertical black dotted line denotes the $k_y = 0$ line that (a) is plotted for. (c), (d) (c) The admittance spectrum and (d) logarithm of the band gap for the system in (a) in a nanowire geometry with OBC along the x and y directions and PBCs along the z direction. The horizontal black lines in (c) and (d) denote the k_z values of the bulk Weyl points. Gap-closing chiral hinge states are evident in the admittance spectrum in (c) at the k_z range where no surface states exist in the nanoplate geometry. The presence of these chiral states is further corroborated by the small magnitudes of the band gap for all values of k_z. (e)–(h) The counterparts of (a)–(d) for a system with the same parameters as (a)–(d) except that R_c now has a finite value of 0.2 mF. The common parameters are $C_1 = 2.5$ mF, $C_2 = 2$ mF, $C_z = 0.4$ mF, $R_1 = 1.414$ mF, and $C_t = 0$ mF.

may undergo multiple or no phase transitions as k_z is varied while the other parameters are fixed. Fig. 7(a) shows the k_z–C_1 phase diagram for a parameter set that encompasses those in Figs. 5(a)–5(d) and 6(a)–6(d). For this set of parameters, there are at zero or two WPs at each value of C_1, and the QTI (quadrupole TI) regions on the C_1–k_z plane are sandwiched by the 1CI (first-order Chern insulator) regions. The phase transitions that occur with the variation of k_z in this system therefore occur only between the 1CI and topologically trivial phases, for example, at $C_1 = -1$ mF as shown in Fig. 5, or between the QTI and 1CI phases, for example, at $C_1 = 2.5$ mF as shown in Fig. 6. There are also values of C_1 at which there there are no WPs and hence no phase transitions, such as in the $C_1 = 2$ mF case shown in Figs. 7(b) and 7(c), which is a 1CI phase for all values of k_z. Figure 7(b) shows that there are two topological zero modes on the $k_y = 0$ line belonging to two pairs of surface-state bands that are separated along the k_z axis in this case when a nanoplate geometry is imposed on the system, while the large magnitudes of the band gap in the nanowire geometry in Fig. 7(c) show that there are no second-order hinge states in the system. Figure 7(e) shows the phase diagram for another set of parameters for which there may now be multiple pairs of WPs at different values of k_z for a given value of C_1. For example, Fig. 7(d) and the projections of the WPs on the k_y–k_z plane in Fig. 7(e) show that as k_z is varied from π to 0 at $C_1 = 1.5$, three WPs at $k_y = 0$ or $k_y = \pm\pi$ are crossed, between which the system switches from the 1CI to the QTI phase, QTI phase back to the 1CI phase, and the 1CI phase to the topologically trivial phases. These phases are corroborated by the magnitudes of the band gaps for the nanoplate geometry in Fig. 7(e), where dark blue spots corresponding to surface state topological

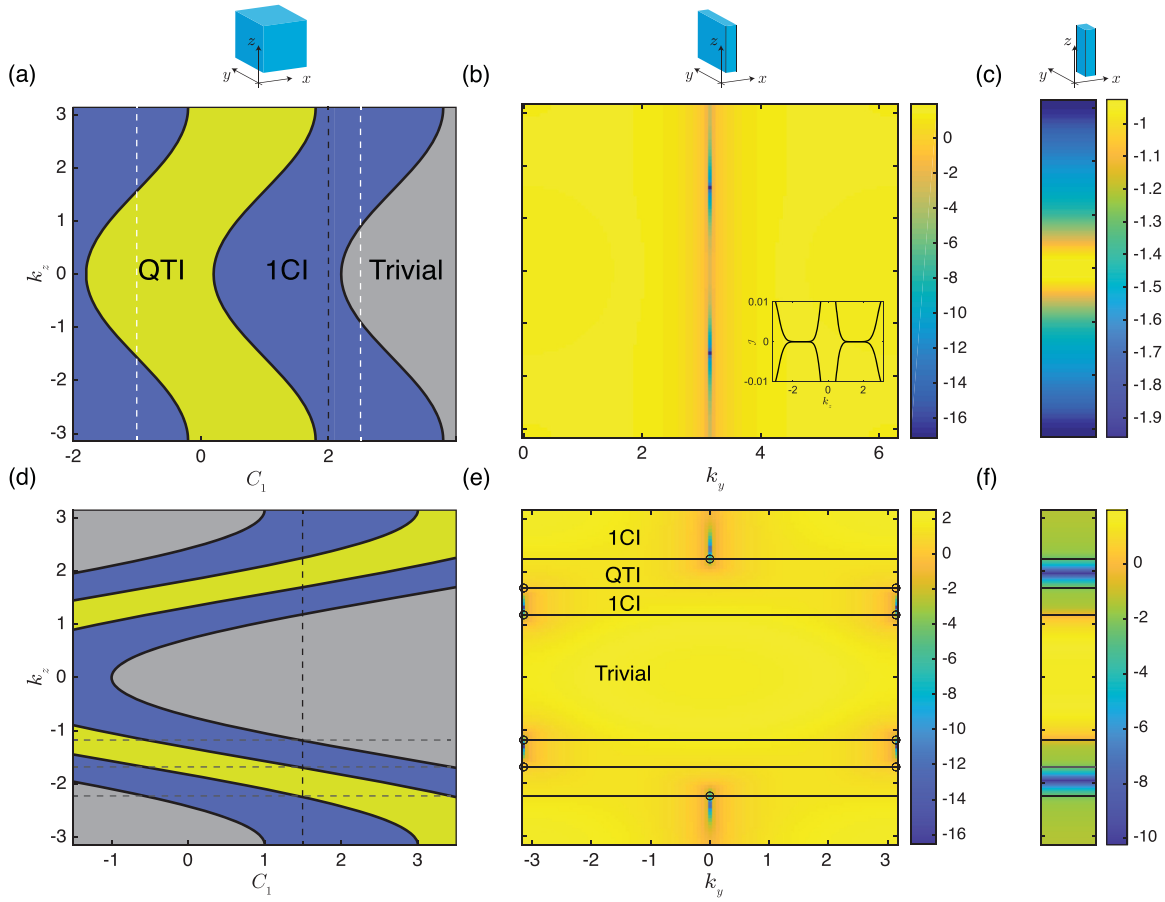

FIG. 7. k_z–C_1 plane phase diagram. (a) Phase diagram for a system with $C_2 = 2$ mF, $C_z = 0.4$ mF, $R_1 = 1.414$ mF, and $C_t = R_c = 0$ mF. The trivial (gray), first-order Chern insulator (1CI, blue), and second-order quadrupole TI (QTI, green) phases are denoted in different colors. The black lines at the boundaries between the different phases denote the k_z values of the bulk WPs at the given value of C_1. The vertical white dotted lines at $C_1 = -1$ and $C_1 = 2.5$ mF denote the first- and second-order WP systems shown in Figs. 5 and 6, respectively, while the black dotted line at $C_1 = 2$ mF denotes the C_1 value of 1CI phase shown in Fig. 6. (b) The logarithm of the band gap for an exemplary first-order Chern insulator system with the parameters shown in (a) and $C_1 = 2$ mF in a nanoplate geometry with OBCs along the x direction and PBCs along the y and z directions. There are two topological-zero energy states indicated by the dark blue spots on the $k_y = \pi$ line indicated by the white dotted line. The inset shows the dispersion of the surface states at $k_y = \pi$ plotted on a linear admittance scale. There are no bulk WPs for this parameter set. (c) The logarithm of the band gap when a nanowire geometry with OBCs along the x and y directions are imposed on the system and PBCs along the z direction. The large magnitudes of the band gap indicate the absence of higher-order hinge states in the system. (d) The phase diagram for a system with $C_2 = 2$ mF, $C_z = 2$ mF, $R_1 = 1.414$ mF, and $C_t = R_c = 0$ mF. The black dotted line at $C_1 = 1.5$ denotes the C_1 value of the system hosting both first- and second-order WPs in (e). (e) The logarithm of the band gap for an exemplary first-order Chern system with the parameters shown in (d) and $C_1 = 1.5$ mF in a nanoplate geometry with OBCs along the x direction and PBCs along the y and z directions. The black dotted lines indicate the k_z values of the bulk WPs, the projections of which on the k_y–k_z plane are indicated by the circles. These lines form the boundaries between regions where surface states, indicated by the dark blue streaks corresponding to small values of band gaps, are present or not present. (f) The logarithm of the band gap for a nanowire geometry with OBCs along the x and y directions and PBCs along the z direction. The very small magnitudes of the band gaps around $k_z \approx \pm 2$ indicate the presence of hinge state zero modes at these k_z values.

zero modes are present in the 1CI k_z ranges bounded by the WPs, and by the small magnitudes of the band gaps for the nanowire geometry in Fig. 7(f), corresponding to topological zero modes of the hinge states in the QTI phase in k_z ranges sandwiched between those of the 1CI phase. This system is therefore a hybrid chiral hinge system that hosts both first- and second-order WPs simultaneously.

In summary, we have realized both topological first- and second-order chiral states and Weyl semimetallic phases by varying electrical resistive parameters in a TE circuit without the requirement of any external magnetic fields. Higher-order topologically nontrivial systems (which include topological insulators and Weyl and Dirac semimetals) host distinct hinge states that are expected to be robust against perturbations because the direction of their propagation is locked to their pseudospin. They are also applicable to the study of Majorana fermions, which are actively being investigated for applications in fault-tolerant quantum computing [77]. This robust unidirectional property, in which current flow is allowed in only one direction along a hinge, implies that a chiral hinge current excited at one hinge in a cuboid circuit cannot flow into another hinge situated diagonally opposite from the hinge

being excited [78,83]. This property can therefore be exploited for robust topological signal multiplexing by utilizing the multiple discrete degrees of freedom in the system [79]. Finally, HOWSM states with hinge states open the possibility for robust dissipationless interconnects [67] and analogs of truly 1D superconducting nanowires [84].

III. CONCLUSION

In this paper, we proposed a tunable scheme to realize various topological and chiral phases in a TE network consisting of basic electrical components such as resistors, inductors, and capacitors. We first constructed the circuit model for a 2D quadrupole topological insulator using these basic components. We then extended the original 2D TE circuit in the vertical z direction by stacking copies of the 2D circuits one on top of another. By coupling the nodes in adjacent layers diagonally using a common stacking capacitor C_z, we can modulate the intra- and intercell coupling of the effective 2D Laplacian to realize a richer set of topological properties associated with gapless states in 3D. For instance, we obtained a flat band with higher-order hinge states that connect two gapless nodes together. The gapless nodes exhibit Dirac or Weyl semimetalic characteristics depending on the circuit symmetries. Interestingly, the chiral symmetry of the hinge states can be broken by adding resistive couplings between equivalent nodes on adjacent layers. In this case, two hinge states survive and propagate with positive and negative group velocities in the z direction. Furthermore, by incorporating tilting capacitances, both chiral modes in a given valley can be made to propagate in the same direction but opposite to that of the corresponding modes in the other valley. The flat-band edge and hinge states in these 3D layered TE circuits may find applications in sensors with high sensitivity and ultralow dissipation, owing to their tunability and chirality.

ACKNOWLEDGMENTS

This paper is supported by the Ministry of Education (MOE) of Singapore Tier-II Grant No. MOE-T2EP50121-0014 (NUS Grant No. A-8000086-01-00) and a MOE Tier-I FRC grant (NUS Grant No. A-8000195-01-00).

S.M.R-U-I., Z.B.S, H.S, and M.B.A.J initiated the primary idea. S.M.R-U-I. and Z.B.S contributed to the formulation of the analytical model, code development, data analysis, and to the writing of the paper under the kind supervision of M.B.A.J

The authors declare no competing interests.

APPENDIX

1. Negative resistance converter with current inversion and dynamic stability of op-amps

To induce a negative imaginary on-site potential (i.e., gain term) in the TE circuit array, we use the unity gain operational amplifier (op-amp) circuit shown in Fig. 8 to provide an additional π phase modulation with respect to the original resistance value. The circuit comprises two feedback capacitors with the same capacitance C_a, an operational amplifier, and a resistance R. The relation between the input current and the voltage along the forward (node p to q) and backward (node q to p) directions can be expressed in the matrix form

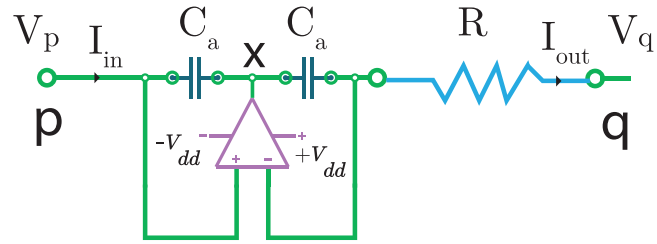

FIG. 8. Illustration of a simple negative resistance converter with current inversion.

$$\begin{pmatrix} I_{pq} \\ I_{qp} \end{pmatrix} = \frac{1}{R}\begin{pmatrix} -1 & 1 \\ -1 & 1 \end{pmatrix}\begin{pmatrix} V_p \\ V_q \end{pmatrix}, \tag{A1}$$

where I_{ij} and V_i denote the current passing from the ith to the jth node and the voltage at the ith node respectively. From Eq. (A1), we can easily obtain

$$I_{pq} = -I_{qp} = -\frac{V_p - V_q}{R}. \tag{A2}$$

Therefore, for the coupling from node p to q, the resistance will acquire a phase of π relative to the coupling from node q to p, and behave as a negative resistor with a value of $-R$. If we replace the resistance by an inductance or capacitance or a combination of a resistance and capacitance, Eq. (A1) translates to a general schematic of a negative impedance converter with current inversion.

2. Topological invariants

a. Winding number

As explained in the main text, the circuit Laplacian described in Eq. (1) at resonant frequency but without tilting capacitance (i.e., $C_t = 0$) respects both chiral and mirror rotational symmetry around the xy plane. The Laplacian can therefore be transformed into a block diagonal form along a high symmetry line (i.e., $k_x = k_y = k$) after a simple unitary transformation,

$$\chi^{-1} Y(\omega_r, k, k_z)\chi = \begin{bmatrix} Y_1(\omega_r, k, k_z) & 0 \\ 0 & Y_2(\omega_r, k, k_z) \end{bmatrix}, \tag{A3}$$

where $Y_1(\omega_r, k, k_z)$ and $Y_2(\omega_r, k, k_z)$ are given by

$$Y_1(\omega_r, k, k_z) = (C_1 + 2C_z \cos k_z + C_2 \cos k)\sigma_x + C_2 \sin k\sigma_y \tag{A4}$$

and

$$Y_2(\omega_r, k, k_z) = (C_1 + 2C_z \cos k_z + C_2 \cos k)\sigma_x - C_2 \sin k\sigma_y, \tag{A5}$$

and χ is the unitary transformation matrix. If we consider k_z as a tunable parameter, the winding number of $Y_1(\omega_r, k, k_z)$

can be obtained explicitly as

$$\begin{aligned}\mathcal{W}_1 &= -\frac{i}{2\pi}\oint \psi^\dagger \partial_k \psi \, \mathrm{d}k \\ &= \frac{1}{2\pi}\int_{k=0}^{k=2\pi} \mathrm{d}k \left[\tan^{-1}\left(\frac{\sin k}{\frac{C_1+2C_z\cos k_z}{C_2}+\cos k}\right)\right] \\ &= \theta(C_2-(C_1+2C_z\cos k_z)), \end{aligned} \tag{A6}$$

where θ is the Heaviside step function and ψ is the eigenstate of $Y_1(\omega_r, k, k_z)$. Similarly, the winding number of $Y_2(\omega_r, k, k_z)$ can be calculated as

$$\mathcal{W}_2 = -\theta(C_2-(C_1+2C_z\cos k_z)). \tag{A7}$$

Therefore, the resultant winding number of the 4×4 matrix in Eq. (1) is given by

$$\mathcal{W} = \mathcal{W}_1 - \mathcal{W}_2 = \begin{cases} 2, & \text{if } \left|\frac{C_1+2C_z\cos k_z}{C_2}\right| \leqslant 1 \\ 0, & \text{otherwise,} \end{cases} \tag{A8}$$

as shown in Eq. (10).

b. Chern number

For a quasi-2D system where k_z is treated as a tunable parameter rather than a spatial dimension, the Chern number C at given value of k_z is given by

$$C(k_z) = \frac{1}{2\pi}\int \mathrm{d}^2k \ \mathrm{Tr}\left(\partial_{k_x}A_{k_y}(k_x,k_y;k_z) - \partial_{k_y}A_{k_x}(k_x,k_y;k_z)\right), \tag{A9}$$

where A is the Berry curvature matrix in which the (m,n)th element, $[A_{k_i}]^{m,n}$, is given by $[A_{k_i}]^{m,n} = \langle u^{(m)}(k_x,k_y,k_z)|\partial_{k_i}u^{(n)}(k_x,k_y,k_z)\rangle$, and $|u^{(m)}(k_x,k_y,k_z)\rangle$ is the mth eigenvector of the bulk Laplacian matrix Eq. (1).

c. Quadrupole TI index

Treating k_z as a tunable parameter rather than a spatial dimension, the quadrupole TI index for our system can be defined by a pair of integers $\mathbf{p}(k_z) = (p_x(k_z), p_y(k_z))$ in which

$$p_x(k_z) = -\frac{1}{2\pi^2}\int \mathrm{d}k \ \mathrm{Tr}\big(\tilde{A}_{k_y}(k_x,k_y;k_z)\big), \tag{A10}$$

$$p_y(k_z) = -\frac{1}{2\pi^2}\int \mathrm{d}k \ \mathrm{Tr}\left(\tilde{A}_{k_x}(k_x,k_y;k_z)\right). \tag{A11}$$

Here,

$$\left[\tilde{A}_{k_y}\right]^{j,j'} = -i\big\langle w_x^j(k_x,k_y;k_z)\big|\partial_{k_y}w_x^j(k_x,k_y;k_z)\big\rangle, \tag{A12}$$

$$\left[\tilde{A}_{k_x}\right]^{j,j'} = -i\big\langle w_y^j(k_x,k_y;k_z)\big|\partial_{k_x}w_y^j(k_x,k_y;k_z)\big\rangle, \tag{A13}$$

and the $|w^j_{(x,y)(k_x,k_y;k_z)}\rangle$s are, in turn, the eigenvectors of the Wannier bands below the Wannier gap. For the 4×4 system considered here, $|w^j_{x(k_x,k_y;k_z)}\rangle$ is given by the eigenvector with the smaller eigenvalue of

$$\begin{aligned} &W_x(k_x,k_y;k_z) \\ &= \lim_{N_y\to\infty}\prod_{n_y=1}^{N_y}\left(\sum_{j,j'\in\mathrm{occ}}\left|u^{(j)}\left(k_x,k_y\right.\right.\right. \\ &\quad \left.\left.\left.+\frac{2\pi n_y}{N_y},k_z\right)\right\rangle\left\langle u^{(j')}\left(k_x,k_y+\frac{2\pi(n_y-1)}{N_y},k_z\right)\right|\right), \end{aligned} \tag{A14}$$

where the summation over j and j' runs over only the eigenvectors with the two smallest eigenvalues, and $W_y(k_x,k_y;k_z)$ is defined analogously.

The QTI phase in our system corresponds to one where both $p_x(k_z)$ and $p_y(k_z)$ have nonzero values, and the trival and first-order Chern insulator phases one where both $p_x(k_z)$ and $p_y(k_z)$ are zero.

The data and computer codes that support the plots and other findings of this paper are available from the corresponding author upon reasonable request.

[1] M. Vergniory, L. Elcoro, C. Felser, N. Regnault, B. A. Bernevig, and Z. Wang, Nature (London) **566**, 480 (2019).

[2] S. M. Rafi-Ul-Islam, Z. B. Siu, H. Sahin, C. H. Lee, and M. B. A. Jalil, Phys. Rev. Res. **4**, 013243 (2022).

[3] B. Yan and C. Felser, Annu. Rev. Condens. Matter Phys. **8**, 337 (2017).

[4] Z. Xu, Q. Yuan, Z. B. Siu, S. M. Rafi-Ul-Islam, C. Sun, S. Zhao, and M. B. A. Jalil, J. Phys. D **56**, 065304 (2023).

[5] S. M. Rafi-Ul-Islam, Z. B. Siu, H. Sahin, and M. B. A. Jalil, Front. Phys. **10**, 1021192 (2022).

[6] M. Z. Hasan and C. L. Kane, Rev. Mod. Phys. **82**, 3045 (2010).

[7] X.-L. Qi and S.-C. Zhang, Rev. Mod. Phys. **83**, 1057 (2011).

[8] E. Shimshoni and A. Auerbach, Phys. Rev. B **55**, 9817 (1997).

[9] C. Sun, S M Rafi-Ul-Islam, H. Yang, and M. B. A. Jalil, Phys. Rev. B **102**, 214419 (2020).

[10] Q. L. He, L. Pan, A. L. Stern, E. C. Burks, X. Che, G. Yin, J. Wang, B. Lian, Q. Zhou, E. S. Choi *et al.*, Science **357**, 294 (2017).

[11] B. A. Bernevig and T. L. Hughes, *Topological Insulators and Topological Superconductors* (Princeton University Press, New Jersey, 2013).

[12] M. Sato and Y. Ando, Rep. Prog. Phys. **80**, 076501 (2017).

[13] F. Schindler, A. M. Cook, M. G. Vergniory, Z. Wang, S. S. Parkin, B. A. Bernevig, and T. Neupert, Sci. Adv. **4**, eaat0346 (2018).

[14] M. Ezawa, Phys. Rev. Lett. **120**, 026801 (2018).

[15] Y. Hatsugai, Phys. Rev. Lett. **71**, 3697 (1993).

[16] T. Fujita, M. Jalil, S. Tan, and S. Murakami, J. Appl. Phys. **110**, 121301 (2011).

[17] D. Vanderbilt, *Berry Phases in Electronic Structure Theory: Electric Polarization, Orbital Magnetization and Topological Insulators* (Cambridge University Press, Cambridge, 2018).

[18] J. E. Moore and L. Balents, Phys. Rev. B **75**, 121306 (2007).
[19] L. Tarruell, D. Greif, T. Uehlinger, G. Jotzu, and T. Esslinger, Nature (London) **483**, 302 (2012).
[20] L. Lu, L. Fu, J. D. Joannopoulos, and M. Soljačić, Nat. Photon. **7**, 294 (2013).
[21] S. M. Rafi-Ul-Islam, Z. B. Siu, C. Sun, and M. B. A. Jalil, Phys. Rev. Appl. **14**, 034007 (2020).
[22] B. Q. Lv, H. M. Weng, B. B. Fu, X. P. Wang, H. Miao, J. Ma, P. Richard, X. C. Huang, L. X. Zhao, G. F. Chen, Z. Fang, X. Dai, T. Qian, and H. Ding, Phys. Rev. X **5**, 031013 (2015).
[23] S. Rafi-Ul-Islam, Z. B. Siu, C. Sun, and M. B. Jalil, New J. Phys. **22**, 023025 (2020).
[24] M. M. Vazifeh and M. Franz, Phys. Rev. Lett. **111**, 027201 (2013).
[25] S. M. Young and C. L. Kane, Phys. Rev. Lett. **115**, 126803 (2015).
[26] N. P. Armitage, E. J. Mele, and A. Vishwanath, Rev. Mod. Phys. **90**, 015001 (2018).
[27] S. M. Rafi-Ul-Islam, H. Sahin, Z. B. Siu, and M. B. A. Jalil, Phys. Rev. Res. **4**, 043021 (2022).
[28] K. Zhang, Z. Yang, and C. Fang, Nat. Commun. **13**, 2496 (2022).
[29] S. M. Rafi-Ul-Islam, Z. B. Siu, and M. B. A. Jalil, Phys. Rev. B **103**, 035420 (2021).
[30] T. Hofmann, T. Helbig, F. Schindler, N. Salgo, M. Brzezińska, M. Greiter, T. Kiessling, D. Wolf, A. Vollhardt, A. Kabaši *et al.*, Phys. Rev. Res. **2**, 023265 (2020).
[31] S. Longhi, Phys. Rev. Res. **1**, 023013 (2019).
[32] M. Ezawa, Phys. Rev. B **100**, 045407 (2019).
[33] S. Kempkes, M. Slot, J. van Den Broeke, P. Capiod, W. Benalcazar, D. Vanmaekelbergh, D. Bercioux, I. Swart, and C. M. Smith, Nat. Mater. **18**, 1292 (2019).
[34] B.-Y. Xie, H.-F. Wang, H.-X. Wang, X.-Y. Zhu, J.-H. Jiang, M.-H. Lu, and Y.-F. Chen, Phys. Rev. B **98**, 205147 (2018).
[35] A. A. Zyuzin and A. A. Burkov, Phys. Rev. B **86**, 115133 (2012).
[36] Z. B. Siu, C. Yesilyurt, M. B. Jalil, and S. G. Tan, Sci. Rep. **7**, 4030 (2017).
[37] D. I. Pikulin, A. Chen, and M. Franz, Phys. Rev. X **6**, 041021 (2016).
[38] S.-Y. Xu, I. Belopolski, N. Alidoust, M. Neupane, G. Bian, C. Zhang, R. Sankar, G. Chang, Z. Yuan, C.-C. Lee *et al.*, Science **349**, 613 (2015).
[39] Sayed Ali Akbar Ghorashi, T. Li, and T. L. Hughes, Phys. Rev. Lett. **125**, 266804 (2020).
[40] H.-X. Wang, Z.-K. Lin, B. Jiang, G.-Y. Guo, and J.-H. Jiang, Phys. Rev. Lett. **125**, 146401 (2020).
[41] Q. Wei, X. Zhang, W. Deng, J. Lu, X. Huang, M. Yan, G. Chen, Z. Liu, and S. Jia, Nat. Mater. **20**, 812 (2021).
[42] Z. Wang, D. Liu, H. T. Teo, Q. Wang, H. Xue, and B. Zhang, Phys. Rev. B **105**, L060101 (2022).
[43] S. Borisenko, Q. Gibson, D. Evtushinsky, V. Zabolotnyy, B. Büchner, and R. J. Cava, Phys. Rev. Lett. **113**, 027603 (2014).
[44] B.-Y. Xie, G.-X. Su, H.-F. Wang, H. Su, X.-P. Shen, P. Zhan, M.-H. Lu, Z.-L. Wang, and Y.-F. Chen, Phys. Rev. Lett. **122**, 233903 (2019).
[45] T. Liu, Y.-R. Zhang, Q. Ai, Z. Gong, K. Kawabata, M. Ueda, and F. Nori, Phys. Rev. Lett. **122**, 076801 (2019).
[46] R. Süsstrunk and S. D. Huber, Science **349**, 47 (2015).
[47] Z. Yang, F. Gao, X. Shi, X. Lin, Z. Gao, Y. Chong, and B. Zhang, Phys. Rev. Lett. **114**, 114301 (2015).
[48] M. Lewenstein, A. Sanpera, V. Ahufinger, B. Damski, A. Sen, and U. Sen, Adv. Phys. **56**, 243 (2007).
[49] K. Sun, W. V. Liu, A. Hemmerich, and S. D. Sarma, Nat. Phys. **8**, 67 (2012).
[50] Y. Zhang, Y. Kartashov, L. Torner, Y. Li, and A. Ferrando, Opt. Lett. **45**, 4710 (2020).
[51] Y. Chen, Z.-K. Lin, H. Chen, and J.-H. Jiang, Phys. Rev. B **101**, 041109(R) (2020).
[52] E. Edvardsson, F. K. Kunst, and E. J. Bergholtz, Phys. Rev. B **99**, 081302(R) (2019).
[53] X.-W. Luo and C. Zhang, Phys. Rev. Lett. **123**, 073601 (2019).
[54] S. M. Rafi-Ul-Islam, Z. B. Siu, H. Sahin, and M. B. A. Jalil, Phys. Rev. B **106**, 245128 (2022).
[55] S. M. Rafi-Ul-Islam, Z. B. Siu, H. Sahin, C. H. Lee, and M. B. A. Jalil, Phys. Rev. Res. **4**, 043108 (2022).
[56] S. M. Rafi-Ul-Islam, Z. B. Siu, H. Sahin, Md. S. H. Razo, and M. B. A. Jalil, Phys. Rev. B **109**, 045410 (2024).
[57] L. M. Nash, D. Kleckner, A. Read, V. Vitelli, A. M. Turner, and W. T. Irvine, Proc. Natl. Acad. Sci. USA **112**, 14495 (2015).
[58] N. A. Olekhno, E. I. Kretov, A. A. Stepanenko, P. A. Ivanova, V. V. Yaroshenko, E. M. Puhtina, D. S. Filonov, B. Cappello, L. Matekovits, and M. A. Gorlach, Nat. Commun. **11**, 1436 (2020).
[59] H. Sahin, Z. B. Siu, S. M. Rafi-Ul-Islam, J. F. Kong, M. B. A. Jalil, and C. H. Lee, Phys. Rev. B **107**, 245114 (2023).
[60] T. Helbig, T. Hofmann, S. Imhof, M. Abdelghany, T. Kiessling, L. Molenkamp, C. Lee, A. Szameit, M. Greiter, and R. Thomale, Nat. Phys. **16**, 747 (2020).
[61] S. M. Rafi-Ul-Islam, Z. Bin Siu, and M. B. A. Jalil, Commun. Phys. **3**, 72 (2020).
[62] T. Helbig, T. Hofmann, C. H. Lee, R. Thomale, S. Imhof, L. W. Molenkamp, and T. Kiessling, Phys. Rev. B **99**, 161114(R) (2019).
[63] S. Rafi-Ul-Islam, Z. B. Siu, and M. B. Jalil, Appl. Phys. Lett. **116**, 111904 (2020).
[64] S. Imhof, C. Berger, F. Bayer, J. Brehm, L. W. Molenkamp, T. Kiessling, F. Schindler, C. H. Lee, M. Greiter, T. Neupert *et al.*, Nat. Phys. **14**, 925 (2018).
[65] S. M. Rafi-Ul-Islam, Z. B. Siu, H. Sahin, and M. B. A. Jalil, Phys. Rev. Res. **5**, 013107 (2023).
[66] C. H. Lee, S. Imhof, C. Berger, F. Bayer, J. Brehm, L. W. Molenkamp, T. Kiessling, and R. Thomale, Commun. Phys. **28**, 1 (2018).
[67] T. Hofmann, T. Helbig, C. H. Lee, M. Greiter, and R. Thomale, Phys. Rev. Lett. **122**, 247702 (2019).
[68] S. Rafi-Ul-Islam, Z. B. Siu, and M. B. Jalil, New J. Phys. **23**, 033014 (2021).
[69] J. Bao, D. Zou, W. Zhang, W. He, H. Sun, and X. Zhang, Phys. Rev. B **100**, 201406(R) (2019).
[70] S. Rafi-Ul-Islam, Z. B. Siu, H. Sahin, C. H. Lee, and M. Jalil, arXiv:2108.01366.
[71] X. Zhang, B. Zhang, H. Sahin, Z. B. Siu, S. M. Rafi-Ul-Islam, J. F. Kong, B. Shen, M. B. A. Jalil, R. Thomale, and C. H. Lee, Commun. Phys. **6**, 151 (2023).
[72] S. M. Rafi-Ul-Islam, Z. B. Siu, H. Sahin, C. H. Lee, and M. B. A. Jalil, Phys. Rev. B **106**, 075158 (2022).

[73] B. Roy, Phys. Rev. Res. **1**, 032048(R) (2019).
[74] J. Dong, V. Juričić, and B. Roy, Phys. Rev. Res. **3**, 023056 (2021).
[75] B. J. Wieder, Z. Wang, J. Cano, X. Dai, L. M. Schoop, B. Bradlyn, and B. A. Bernevig, Nat. Commun. **11**, 627 (2020).
[76] Q. Wang, Y. Ge, H.-X. Sun, H. Xue, D. Jia, Y.-J. Guan, S.-Q. Yuan, B. Zhang, and Y. D. Chong, Nat. Commun. **12**, 3654 (2021).
[77] Y. You, D. Litinski, and F. von Oppen, Phys. Rev. B **100**, 054513 (2019).
[78] X. Ni, Z. Xiao, A. B. Khanikaev, and A. Alù, Phys. Rev. Appl. **13**, 064031 (2020).
[79] J. Mei, J. Wang, X. Zhang, S. Yu, Z. Wang, and M.-H. Lu, Phys. Rev. Appl. **12**, 054041 (2019).
[80] A. V. Savin and O. V. Gendelman, Phys. Rev. E **67**, 041205 (2003).
[81] Z. Gong, Y. Ashida, K. Kawabata, K. Takasan, S. Higashikawa, and M. Ueda, Phys. Rev. X **8**, 031079 (2018).
[82] W. A. Benalcazar, B. A. Bernevig, and T. L. Hughes, Phys. Rev. B **96**, 245115 (2017).
[83] R. Okugawa, S. Hayashi, and T. Nakanishi, Phys. Rev. B **100**, 235302 (2019).
[84] J. Langbehn, Y. Peng, L. Trifunovic, F. von Oppen, and P. W. Brouwer, Phys. Rev. Lett. **119**, 246401 (2017).